Supporting Information for "Crustal Structure Beneath the Northern Appalachians and the Eastern Grenville Province"

Omid Bagherpur Mojaver[1], Fiona Darbyshire[1]

[1]Centre de recherche Geotop, Université du Québec à Montréal

Contents of this file

1. Data coverage

Seismic ambient noise data in this study are recorded by 69 broadband stations belonging to 6 different seismograph networks (Table S1). Maps of crossing raypaths for the final processed data sets at all 20 periods used in the tomography are presented in Figure S1. Phase velocities are estimated over a grid of 212 nodes and variations of the azimuthal coverage and path density parameters over the inversion grid are provided in Figures S2-S3. Calculation of path density at the nodes was done by checking if great-circle points separated by 5 km along the rays lie within a 50 km radius around the inversion nodes for the available rays (Figure S2). To assess the azimuthal distribution of the paths, the 50 km radius around each inversion node was divided into 5 degree bins, and the number of bins containing 1 or more rays was counted to calculate the percentage azimuthal coverage (Figure S3).

2. Data set statistics

Figure S4 illustrates statistics for all the measured Empirical Green's Functions (EGFs), all phase velocity (dispersion) measurements, and phase velocities used in the final tomography model. The final phase velocity measurements that were input to the tomographic inversions are limited by both a minimum signal-to-noise ratio (SNR) threshold and vari-

---

Corresponding author: O. Bagherpur Mojaver, Centre de recherche Geotop, Université du Québec à Montréal. Canada. (omid.bagherpur@gmail.com)

able minimum inter-station distance threshold for each period. The minimum SNR threshold for the EGFs was calculated using the formula $\mu - 2\sigma$, where μ is the mean and σ is the standard deviation, for the symmetrized SNR distribution, resulting in a value of 8.8 dB for the final data sets (Figure S4a). The minimum inter-station distance threshold varies for different periods and it is calculated using the formula $\Delta \geq 3\lambda$, where Δ is the interstation distance and λ is the characteristic wavelength measured by multiplying average velocity (km/s) by period (s) for different periods (purple dashed lines in Figure S4b-f).

3. Tomography regularization

The final smoothing and damping values (regularization parameters; Table S2) were decided based on the trade-off curves (model roughness versus data fit; a better fit corresponds to a lower "remaining variance") and visual assessment of the output phase velocity maps. The trade-off curves for the 2ψ and 4ψ surface wave components along with examples of the pertinent phase velocity maps are presented in Figures S5-S6 (see main paper for the isotropic component).

4. Resolution tests

The main influencing parameters on the resolving power of a tomography method include the data coverage (Figures S1-S3), and the inversion regularization parameters (Table S2). To assess the resolution of the phase velocity maps, we present the results of resolution tests at four representative periods of 6, 14, 25, and 40 s.

In addition to the spike tests that are discussed in the main paper, we also conducted four extra spike tests, with no anisotropy, in the form of stripe patterns (Synthetic models

S1-S4; Figure S7). These stripes are along two different directions (S1-S2 along NE-SW, and S3-S4 along NW-SE), and with two widths of 80 km (S2 and S4; similar to the inversion node spacing) and 240 km (S1 and S3). The results for the wider stripes suggest an almost perfect recovery at all periods with some very small reduction of amplitude recovery with increasing period. Recovering the narrower 80 km stripes is, however, more challenging for the tomography. The amplitudes of the anomalies across the Gulf of Saint Lawrence, and in the north, are greatly reduced. Anomaly smearing is observable in the north, and also across the Gulf of Maine, especially evident for the NW-SE trending model S4. Spurious anisotropy is limited to the regions close to the edge of the study area, and it is more evident for the narrow stripes (maximum $\sim$1%).

Two sets of linear gradient resolution tests, with no anisotropy, are carried out along NW-SE (model G1) and NE-SW (model G2) directions (Figure S8). Due to the aperture of the study area and differences of data quality along different paths, anomaly patterns elongated along a certain direction might be better recovered, and linear gradient resolution tests are useful to reveal such observations. Comparing the resolving power for models G1 and G2, they are similarly recovered at the shorter periods (6-12 s), but more oscillatory distortion of the linear features is observed in model G2 than model G1 at longer periods (25-40 s). Some small spurious anisotropy ($<$1%) is observable near the northeast and southern edges of the study area (Gulf of Saint Lawrence and Gulf of Maine).

Surface wave velocity inversions include trade-offs between the isotropic and anisotropic components. In order to estimate the amount of leakage between the isotropic and anisotropic components, we conducted leakage tests by inputting only one component of the final phase velocity model and recovering all the surface wave components (Figures

S9-S10). If the inversion of surface wave velocity was perfectly ideal, the inversion would recover the full input signal (e.g., 2ψ anisotropy only) without any signals for the other surface wave components (e.g., isotropic and 4ψ). Examining the results of these tests are helpful for identifying robust model features, and avoiding overinterpretation. In general, the results of these tests suggest a small leakage between the surface wave velocity component and with a generally increasing effect observable with increasing period. Our observations from these tests are listed below:

• Using only isotropic velocity structure as the synthetic input model (second column in Figures S9-S10), the results at all periods suggest that the patterns of isotropic variations are well-recovered, and anisotropy output (2ψ and 4ψ) is very small. That said, we observe loss of amplitude for the anomaly in the North (centred at 73°W, 48.5°N) at 14-25 s period.

• Using only the 2ψ anisotropy component as the input model (third column in Figures S9-S10), the inversion produces very similar pattern and magnitude of 2ψ anomalies at all periods, and the leakage effect for the 4ψ and isotropic components stays mostly minimal. We observe some spurious isotropic anomaly across northeastern Nova Scotia, and near the northern and southern edges of the study area. Some small spurious 4ψ anomalies are also observable beneath Nova Scotia and across the Gaspé Peninsula at the longer periods (25-40 s).

• Lastly, using only the 4ψ anisotropic velocity heterogeneity as the input model (right column in Figures S9-S10), the inversion recovers the 4ψ variations very well at all periods. Compared to the 2ψ input only tests, the observed spurious isotropic anomalies occur beneath similar regions, but this time they are noticably smaller. Spurious 2ψ signals are

mainly observed across Nova Scotia (6-40 s), beneath the Gulf of Maine (40 s), in the southeast (25-40 s), and the northwest of the study area (25-40 s).

To futher examine the resolution of our anisotropic velocity model, we rotated the final 2ψ inversion output by 90° and used it along with the original isotropic solution as the synthetic input models. Figure S11 presents the results of this test at the four representative periods. The inversion produces very similar output at 06-25 s period, whereas the recovered patterns at 40 s period do not match very well with the input model across the Gulf of Saint Lawrence, and the Gulf of Maine. These two regions are subject to low path density and azimuthal coverage (Figures S2-S3).

5. Phase velocity maps

We obtained reliable phase velocity measurements at periods between 4 s and 50 s from the generated EGFs. The full set of phase velocity maps at these periods are presented in Figures S12-S13.

6. Shear velocity model

Our pseudo-3D shear wave velocity model was constructed from the inversions of the 1D local dispersion curves extracted from the 212 inversion nodes of the phase velocity maps. The resulting shear wave velocity maps at a selection of depths from 1 km to 80 km are presented in Figures S14-S16. We also estimated the Moho depths and thicknesses across the study area using two different proxies (Figure S17). Moho depth locations are calculated by locating the 50% and 85% increase values from typical crustal velocities (at 15-25 km depth) toward typical mantle velocities (at 55-65 km depth) for the 1D shear velocity profiles used to make the final shear velocity maps.

7. Effect of non-uniform noise distribution

Previous ANT studies have mentioned the importance of noise distribution in the reliability of phase velocity measurements (e.g., Bensen et al. 2007). Since the main preassumption in the ANT method is that the ambient seismic noise recorded across the study area should be uniformly distributed, a non-uniform noise distribution could cause the resulting models to be biased, and therefore unreliable (e.g., Tian & Ritzwoller 2015, Yang et al. 2008). The main sources of ambient seismic noise generation are believed to be in the oceans (e.g., Gutenberg 1936). Therefore, the seismic noise distribution for study areas located near coastlines can show significant directional bias due to their geographical position. As our study area likely receives the strongest seismic noise from the nearby Atlantic ocean (Figures 1-2 in the main paper), we designed a test procedure to quantify the effect of non-uniform seismic noise distribution in the measurements of phase velocities.

It is suggested that the measurement bias for EGF data sets with a sufficiently smooth non-isotropic noise distribution is small (e.g., Weaver et al. 2009). The best data coverage in our study area is only provided in the 2013-2015 time window as used in this study (Section 2.1 in the main paper), limiting our investigation of different data set scenarios for finding the smoothest varying non-isotropic noise data. According to our tests, however, a stack number of about 6 months for the noise correlation functions is enough for producing reliable EGFs (Figure S18). With the aim of generating a semi-homogenous collection of EGFs that experience a much weaker directional bias than that observed in the final data sets, we processed 12 different seasonal EGF data sets that were created using different 6 month stacks of noise correlation data. We investigated the signal strength coming from

different directions by calculating SNR values of both causal and acausal signals averaged over 5° azimuthal bins for all the 12 different generated seasonal data sets, and considered a few different statistical parameters for the calculated variations to find out which one of the seasonal data sets suggests the smoothest non-isotropic noise distribution (Figure S19). We found that the EGFs resulting from stacking over the months of May-July (2 sets of 3-month stacks) show the smoothest directional variations; hereafter we call the this data set the "semi-homogenous" data set. Table S3 shows the subjective criteria for our decision of choosing the semi-homogenous data set based on the calculated statistical parameters.

We measured all possible inter-station dispersion curves using the same method and procedure used to measure the dispersion data sets that were input to the final phase velocity model inversions (Sections 2.2 and 2.3 in the main paper). We then extracted only paths that were common between the semi-homogenous and final data sets from the measurements to eliminate the effect of variable path coverage between the two data sets. Therefore, if we invert the two new data sets to obtain results, we should recover similar phase velocity maps at each period. Any difference between the recovered phase velocities at the same period can thus be attributed to the effect of non-isotropic noise distribution in the data. Although this test does not fully quantify the effect of the directional bias in our study (because the semi-homogenous data is not an absolutely homogenous data set), it still gives an acceptable estimation for the non-uniform noise distribution effect.

Figure S20 shows the inversion results for the semi-homogenous and final data sets with the same path coverage at different representative periods. As suggested by this illustration, the main model features are generally well-recovered in both models and

most of the differences occur in areas where the path coverage is not sufficient (e.g. Gulf of Saint Lawrence, and areas on the edge of the path coverage). We find the non-uniform noise distribution effect minimal, generally lower than 0.05 km/s, for periods < 30 s. This range is similar to the range of phase velocity uncertainties, and therefore too small to affect the interpretation of our models. For the longer periods that are mostly sensitive to mantle depths, the difference becomes more considerable (0.1-0.2 km/s), especially in regions with less-ideal path coverage such as areas close to the edges of the phase velocity maps including near the Newfoundland coast, northern Nova Scotia, and Gulf of Maine. In the centre of the study area where the path coverage is the best at all periods, the effect of directional bias stays minimal even for the longest periods (Figure S20). This suggests the underappreciated importance of a sufficient path-coverage in removing the effect of directional bias in the measurement of phase velocity maps in ANT studies. Finally, despite being located in a region that is significantly affected by noise directional bias, we conclude that our final phase velocity measurements are reliable. That said, we note that the resolution test results and maps of path coverage at different periods must be considered in the final interpretations of the observed model features.

References

Bensen, G., Ritzwoller, M., Barmin, M., Levshin, A. L., Lin, F., Moschetti, M., ... Yang, Y. (2007). Processing seismic ambient noise data to obtain reliable broad-band surface wave dispersion measurements. *Geophysical Journal International*, *169*(3), 1239–1260. doi: 10.1111/j.1365-246X.2007.03374.x

Gutenberg, B. (1936). On microseisms. *Bulletin of the Seismological Society of America*, *26*(2), 111–117. doi: 10.1785/BSSA0260020111

Tian, Y., & Ritzwoller, M. H. (2015). Directionality of ambient noise on the Juan de Fuca plate: Implications for source locations of the primary and secondary microseisms. *Geophysical Journal International*, *201*(1), 429–443. doi: 10.1093/gji/ggv024

Weaver, R., Froment, B., & Campillo, M. (2009). On the correlation of non-isotropically distributed ballistic scalar diffuse waves. *The Journal of the Acoustical Society of America*, *126*(4), 1817–1826. doi: 10.1121/1.3203359

Yang, Y., Li, A., & Ritzwoller, M. H. (2008). Crustal and uppermost mantle structure in southern Africa revealed from ambient noise and teleseismic tomography. *Geophysical Journal International*, *174*(1), 235–248. doi: 10.1111/j.1365-246X.2008.03779.x

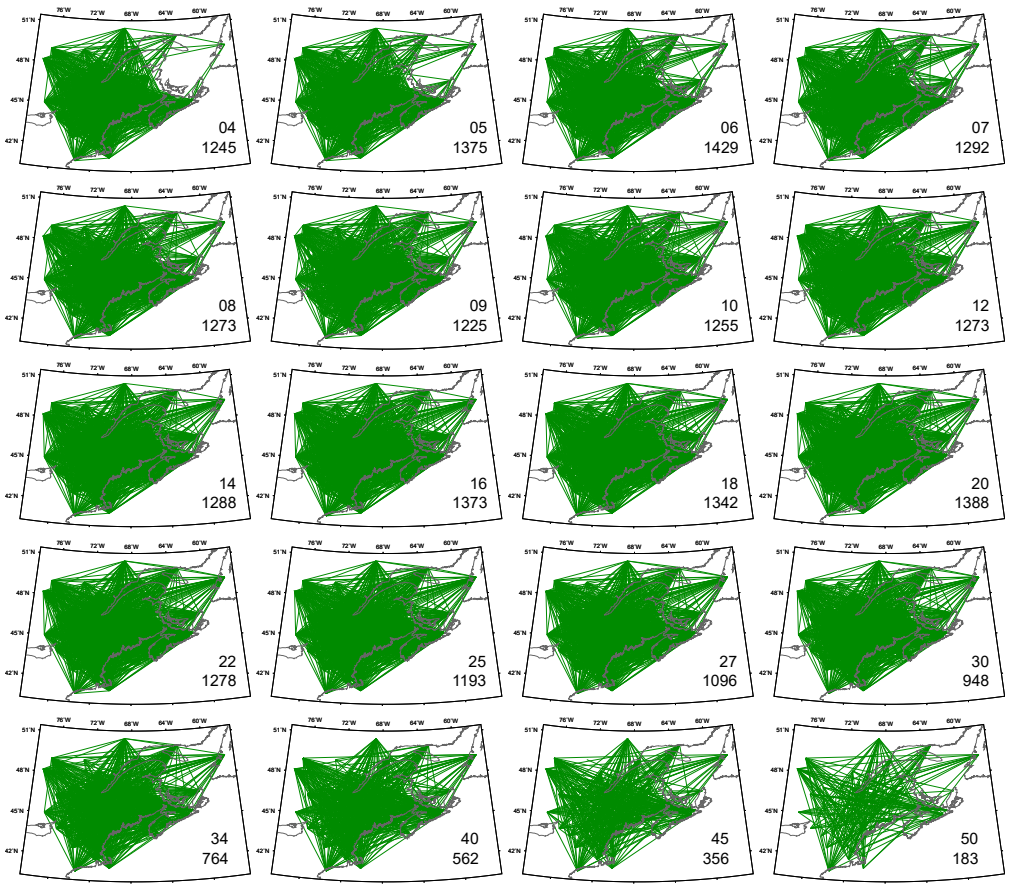

Figure S1. Maps of raypath coverage at all periods in this study. The two numbers at the bottom right of the maps denote the period (s) and the number of rays respectively.

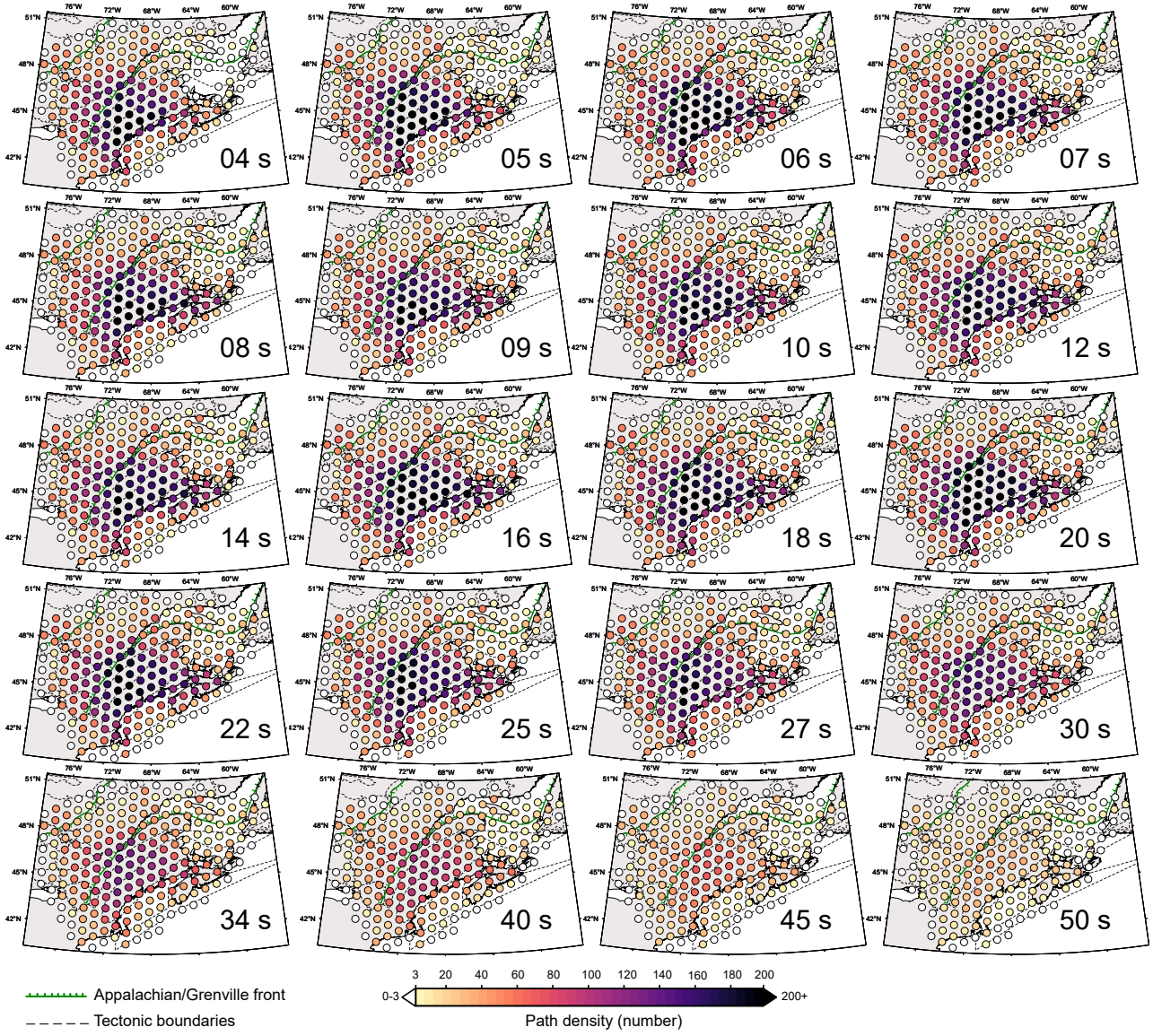

Figure S2. Maps of raypath density at the inversion grid nodes.

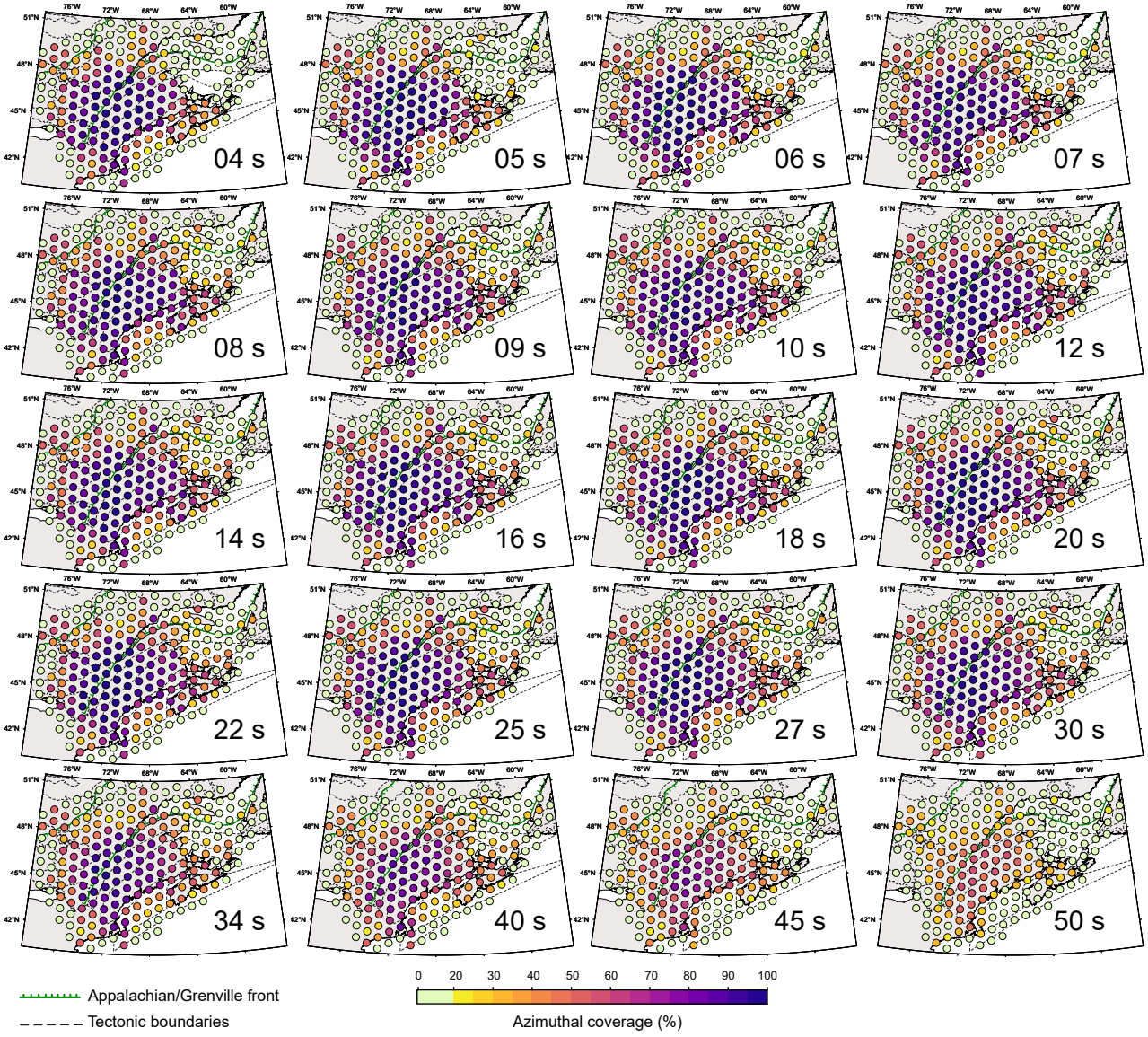

Figure S3. Maps of azimuthal coverage at the inversion grid nodes.

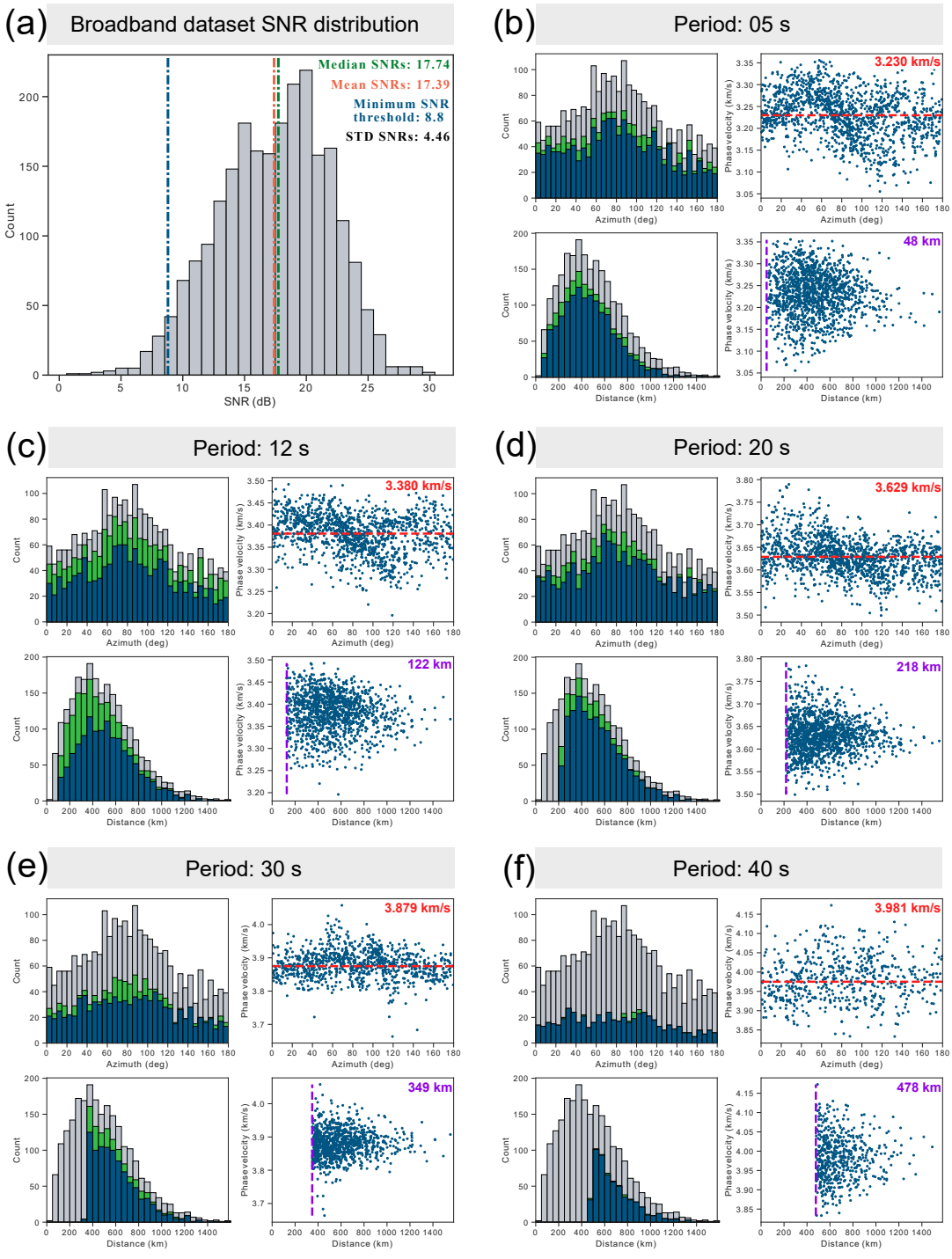

Figure S4. (Caption next page.)

Figure S4. (Previous page.) Statistics for data sets at different processing stages. (a) SNR distribution for the symmetrized EGFs; the blue dashed line shows the minimum SNR threshold for the EGFs (8.8 dB). (b-f) Scatter plots illustrate the final phase velocity measurements used in the tomographic inversions. Color coded histogram plots denote the distribution of data at different data processing stages, including after the generation of EGFs (gray), after inter-station dispersion measurements (green), and final measurements used as the inputs to the tomography (dark blue).

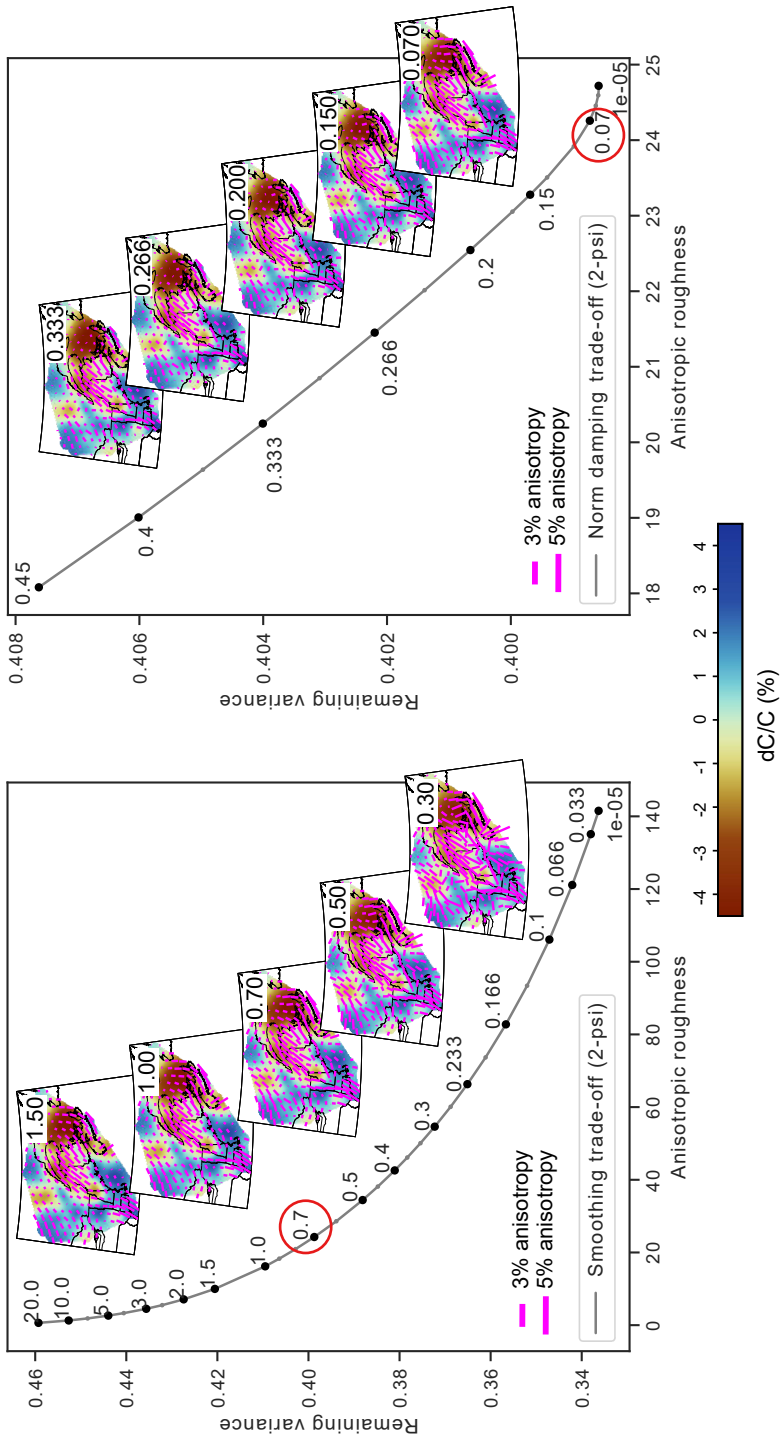

Figure S5. Inversion regularization trade-off curves for 2ψ component at 16 s period. (left) smoothing trade-off curve; (right) damping trade-off curve. The red circles mark the values used in the final inversions. The maps illustrate the inversion results for the regularization parameter values marked at the top right corner of the maps.

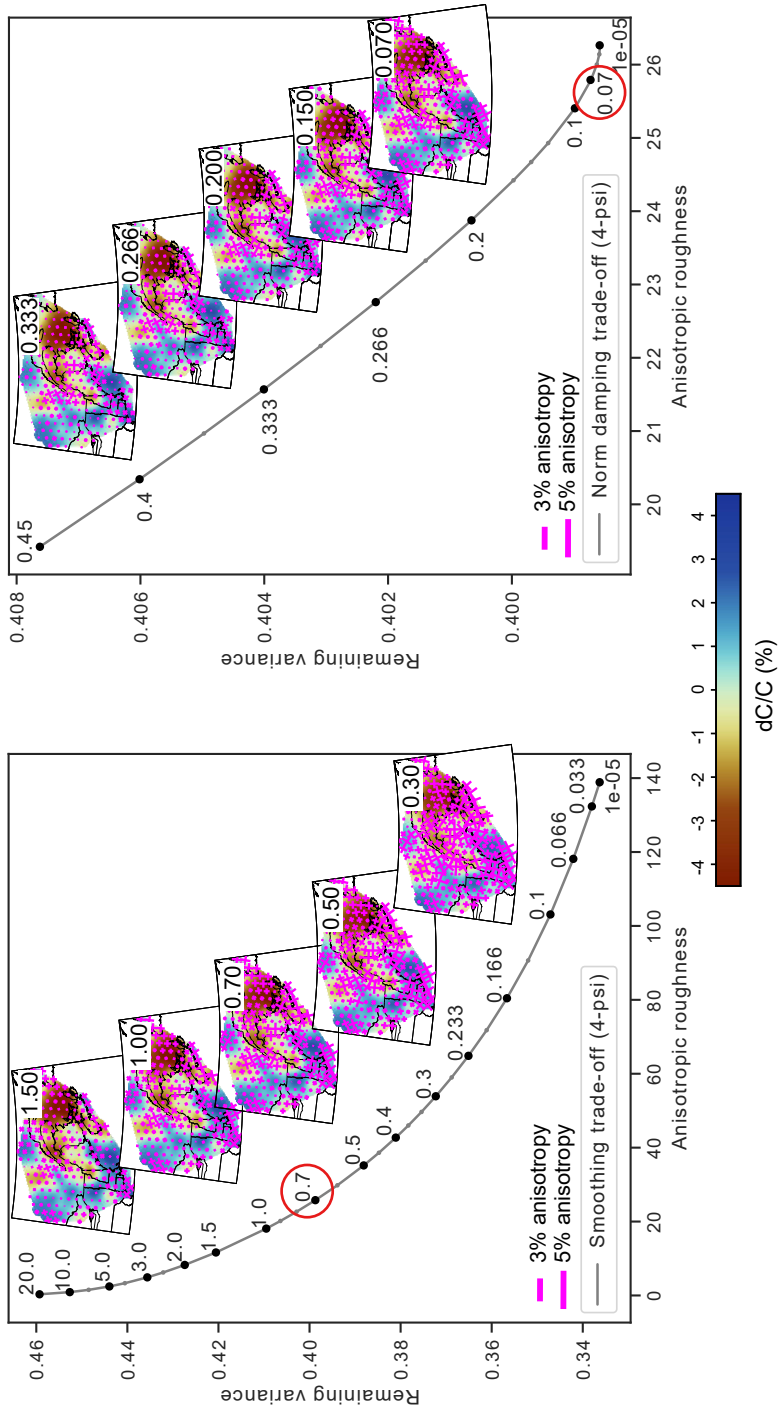

Figure S6. Inversion regularization trade-off curves for 4ψ component at 16 s period. (left) smoothing trade-off curve; (right) damping trade-off curve. The red circles mark the values used in the final inversions. The maps illustrate the inversion results for the regularization parameter values marked at the top right corner of the maps.

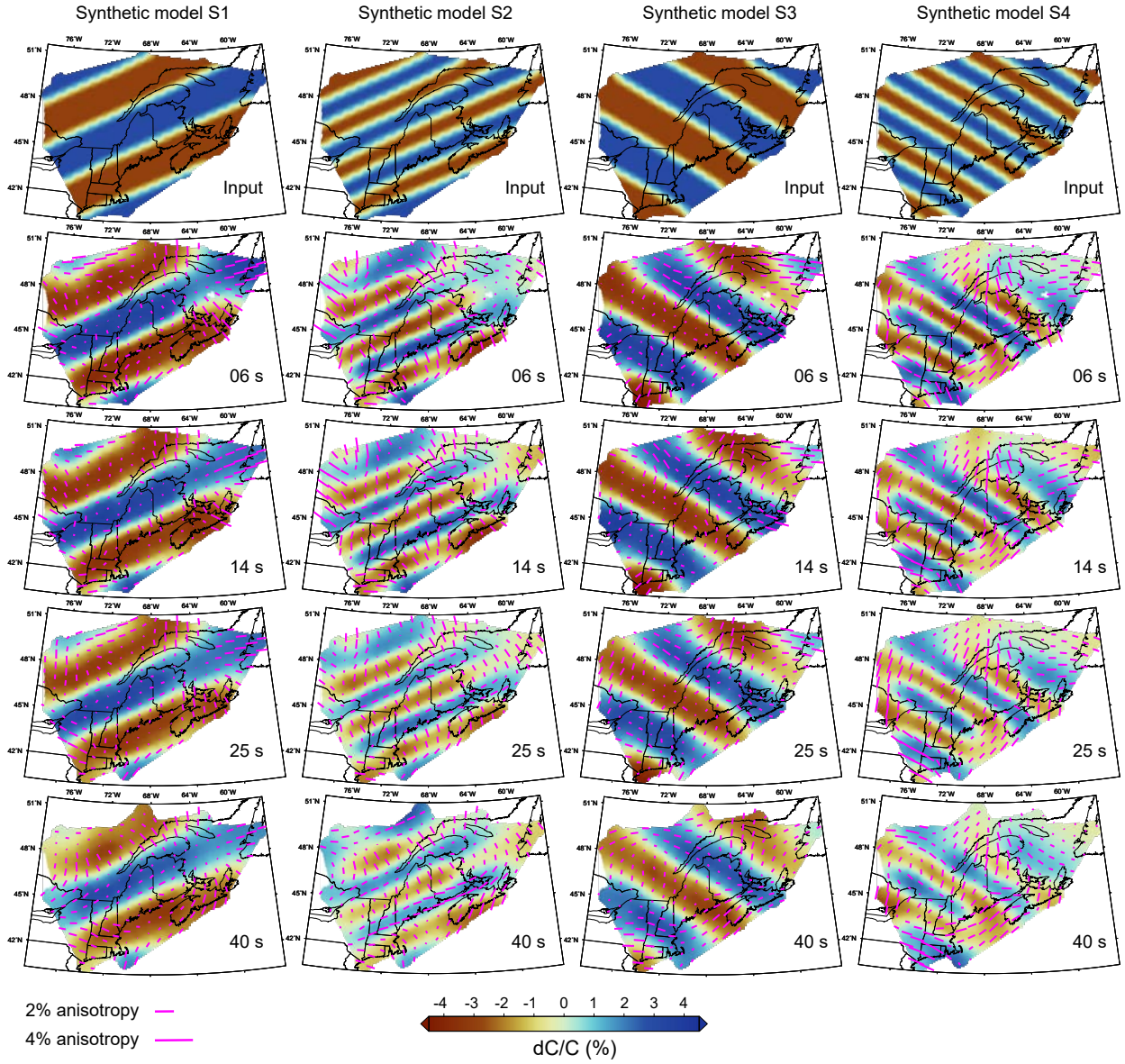

Figure S7. Results for stripe resolution tests for the 4 representative periods (marked at the bottom right of the maps). Tests are carried out for stripes along the main tectonic trend (synthetic models S1-S2), and stripes perpendicular to the trend (synthetic models S3-S4). The stripe widths for the narrow and wide patterns are 80 km and 240 km respectively.

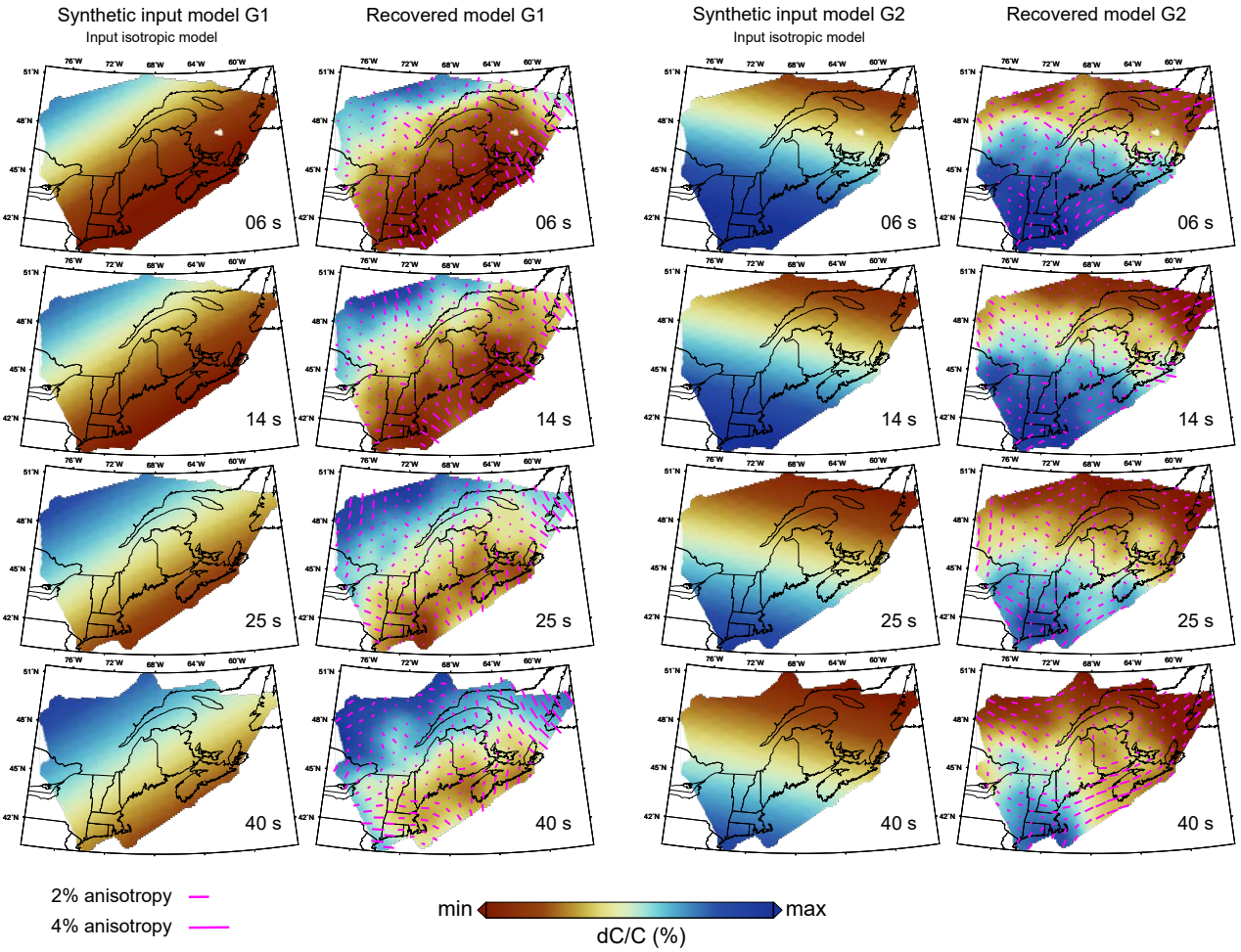

Figure S8. Two sets of gradient resolution tests for the 4 representative periods (model G1: columns 1-2; model G2: columns 3-4), in which a smooth isotropic gradient synthetic model is input to the inversions with the same path coverage and inversion parameters as applied to the real data.

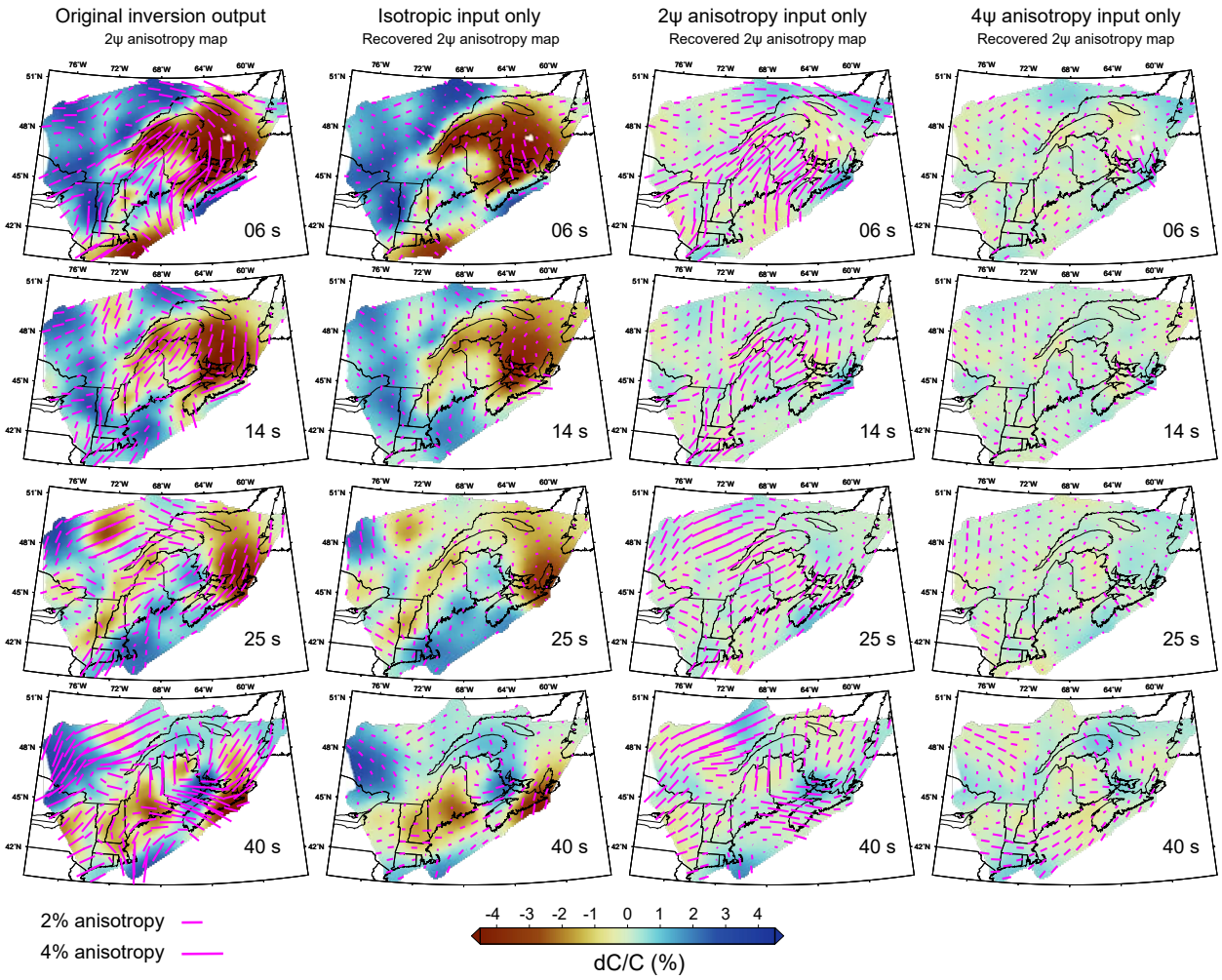

Figure S9. Leakage tests for the 4 representative periods. The isotropic and 2ψ components of the original inversion outputs are shown in the left-hand column. The three right-hand columns illustrate the results for cases where either isotropic, 2ψ, or 4ψ are used as inputs to generate the synthetic models to be recovered using the same path coverage and inversion parameters as used in the real data.

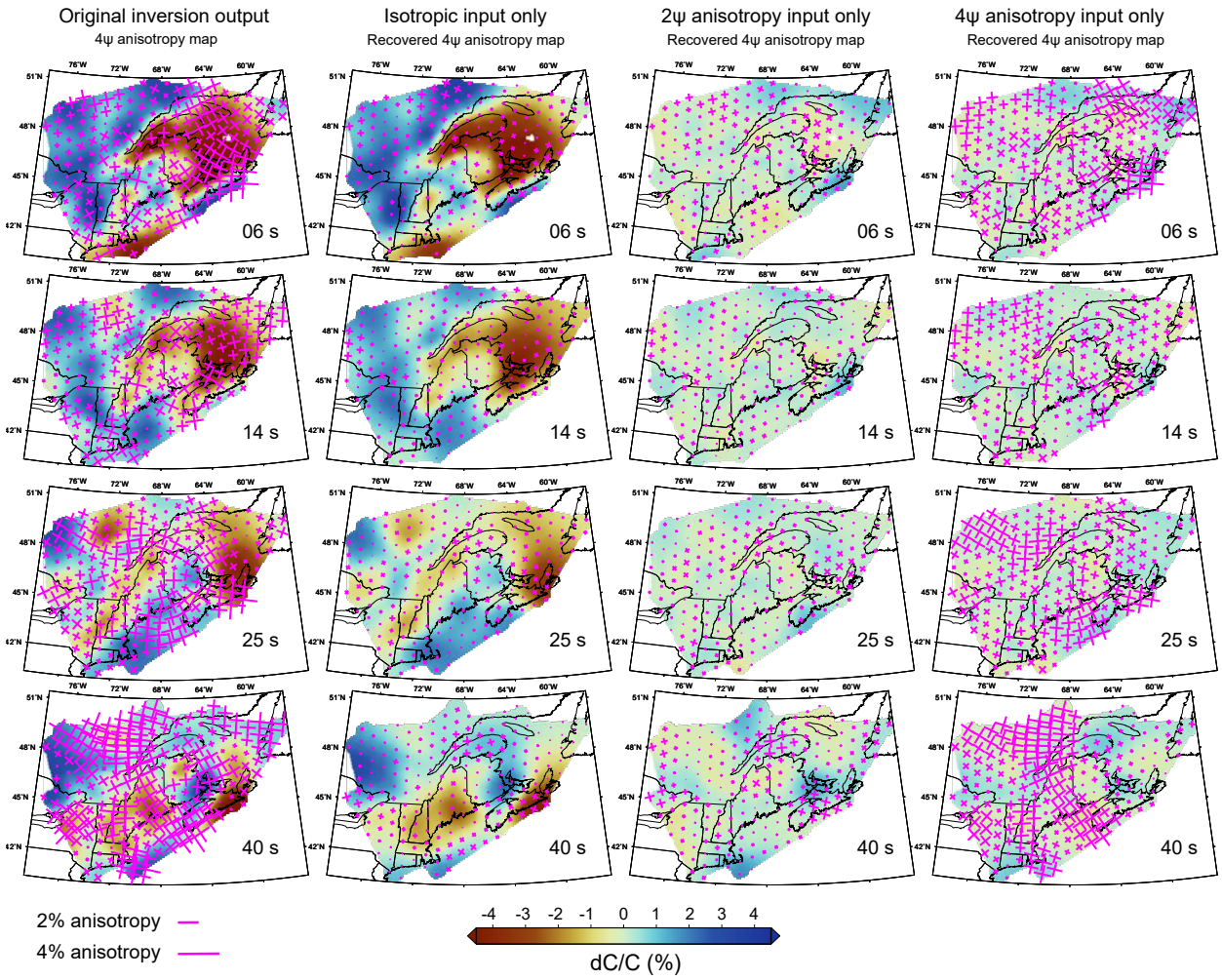

Figure S10. Leakage tests for the 4 representative periods. The isotropic and 4ψ components of the original inversion outputs are shown in the left-hand column. The three right-hand columns illustrate the results for cases where either isotropic, 2ψ, or 4ψ are used as inputs to generate the synthetic models to be recovered using the same path coverage and inversion parameters as used in the real data.

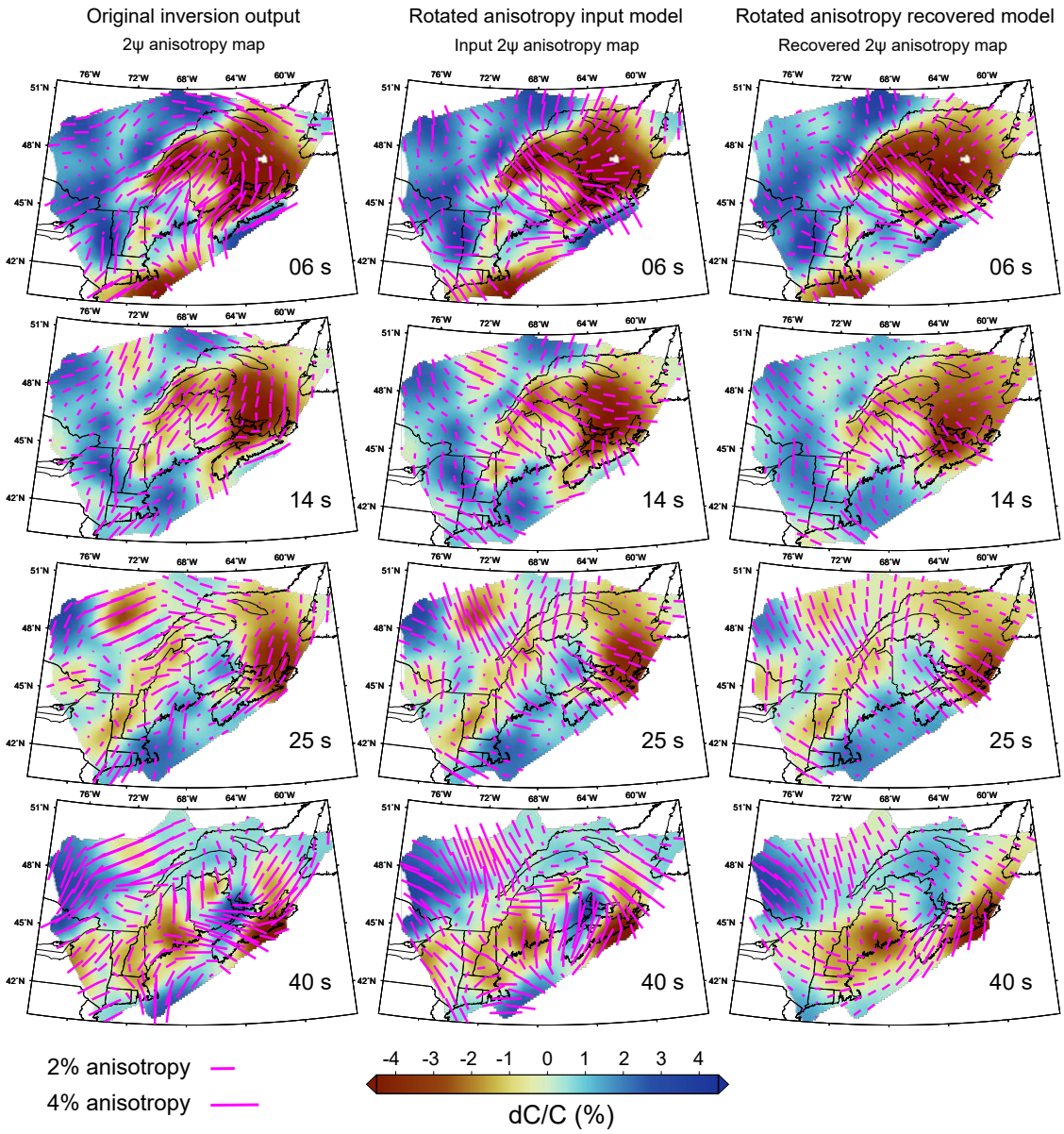

Figure S11. Rotated anisotropy resolution tests for the 4 representative periods, in which the 2ψ anisotropy variations from the original inversion results (first column) are rotated by 90°, and then used as the synthetic input model (second column). The resulting recovered models are shown in the third column.

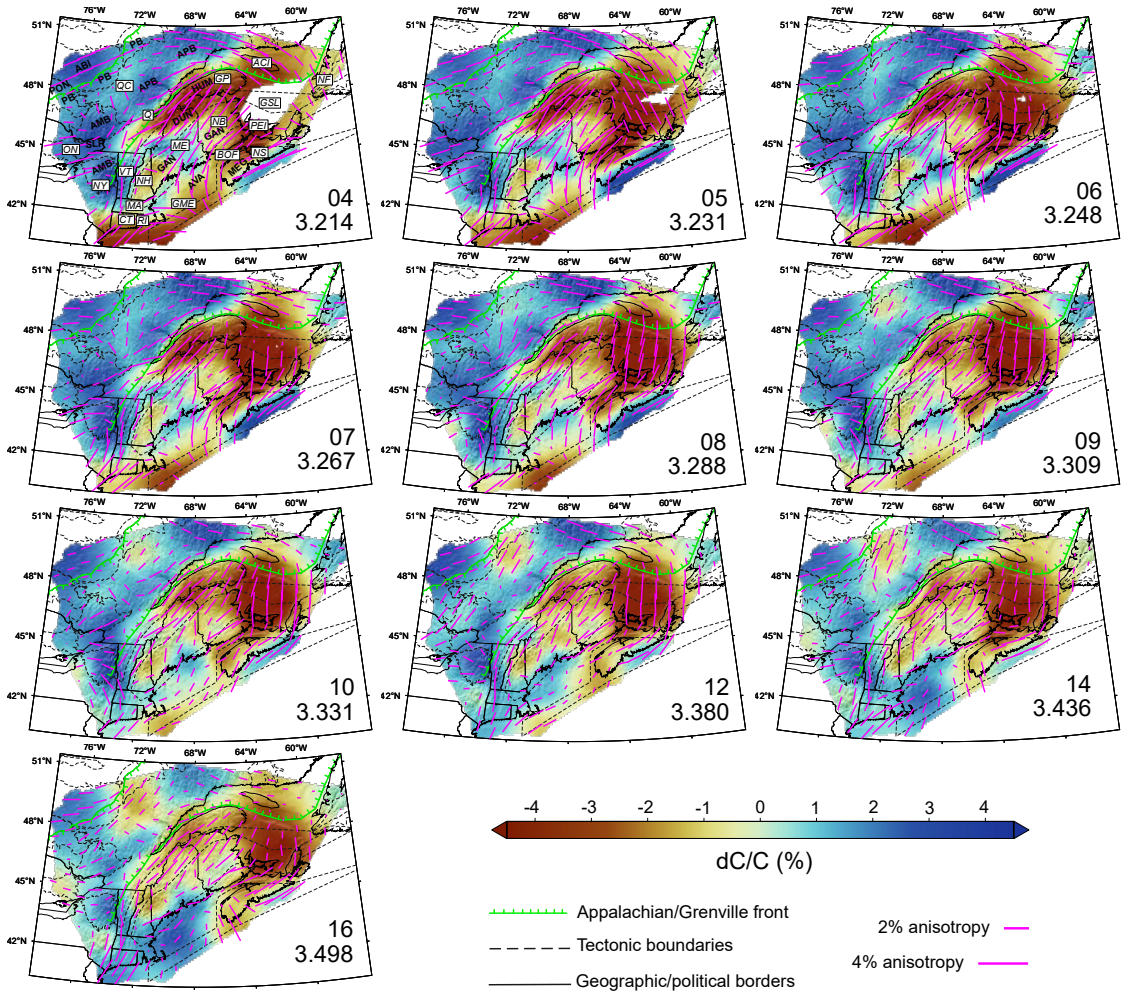

Figure S12. (Caption next page.)

Figure S12. (Previous page.) Final phase velocity maps at 4-16 s period. The two numbers at the bottom right corner of the maps denote period (s) and the average phase velocity (km/s) respectively. Tectonic features: ABI, Abitibi subprovince; AMB, Allochthonous Monocyclic Belt; APB, Allochthonous Polycyclic Belt; AVA, Avalonia; DUN, Dunnage zone; GAN, Ganderia; HUM, Humber margin; MEG, Meguma; PB, Parautochthonous Belt; PO, Pontiac domain; SLP, St. Lawrence platform. Geographic features: ACI, Anticosti Island; BOF, Bay of Fundy; CT, Connecticut; GME, Gulf of Maine; GP, Gaspé Peninsula; GSL, Gulf of St. Lawrence; MA, Massachusetts; ME, Maine; NB, New Brunswick; NF, Newfoundland; NH, New Hampshire; NS, Nova Scotia; NY, New York; ON, Ontario; PEI, Prince Edward Island; Q, Quebec City; QC, Quebec (province); RI, Rhode Island; VT, Vermont.

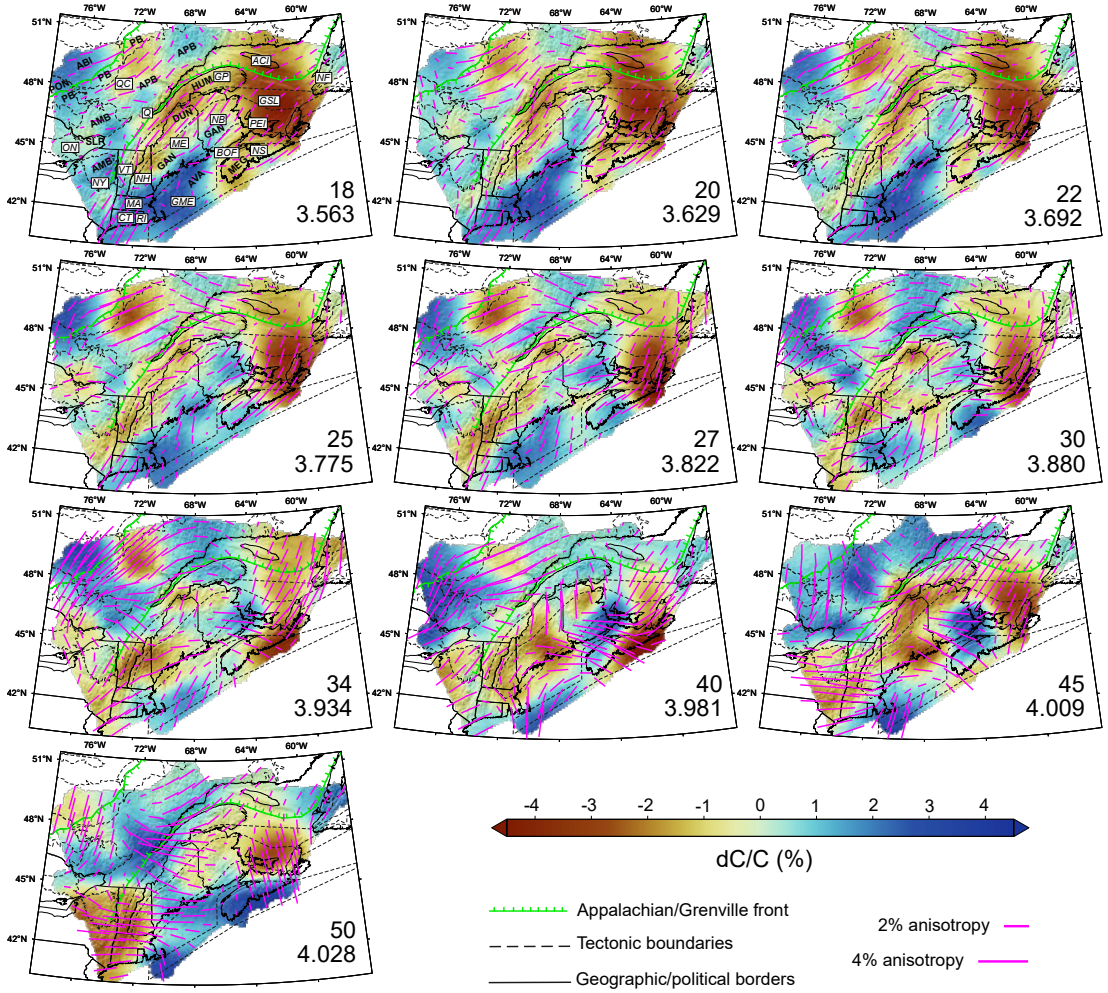

Figure S13. Final phase velocity maps at 18-50 s period. The numbers at the bottom right corner of the maps denote period (s) and the average phase velocity (km/s) respectively. Acronyms are explained in Figure S12.

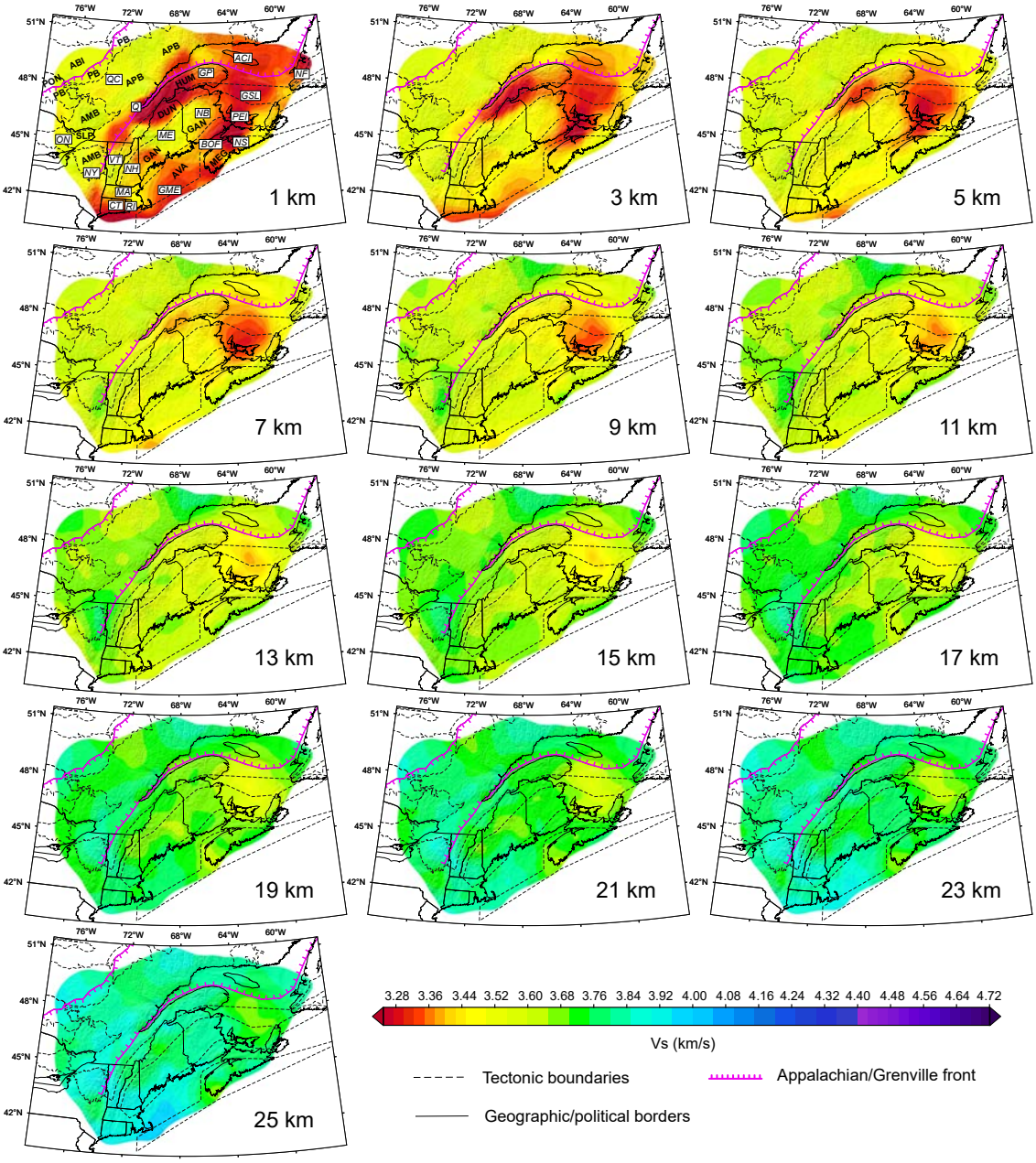

Figure S14. Maps of shear velocity variations at depths from 1 km to 25 km. Acronyms are explained in Figure S12.

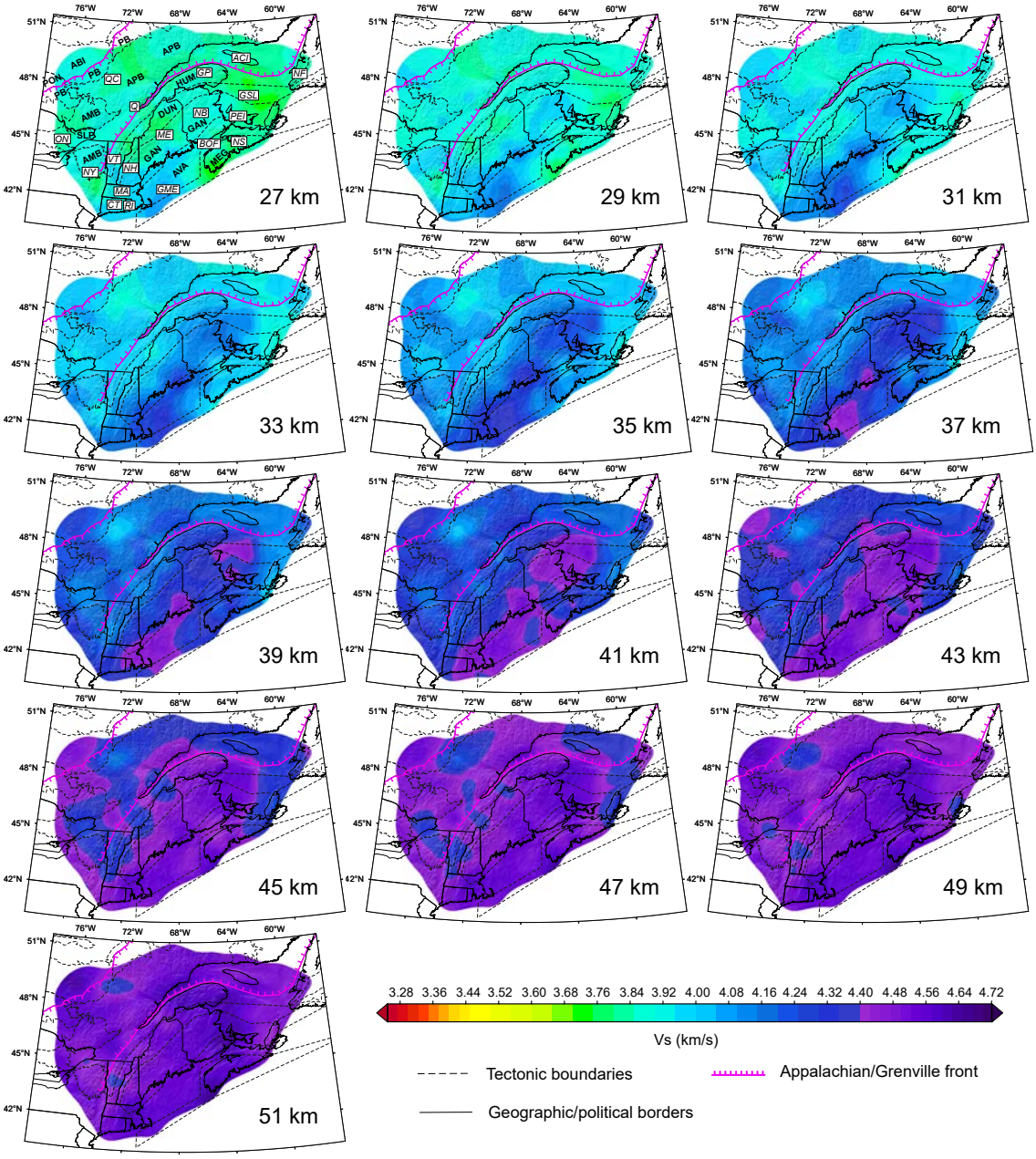

Figure S15. Maps of shear velocity variations at depths from 27 km to 51 km. Acronyms are explained in Figure S12.

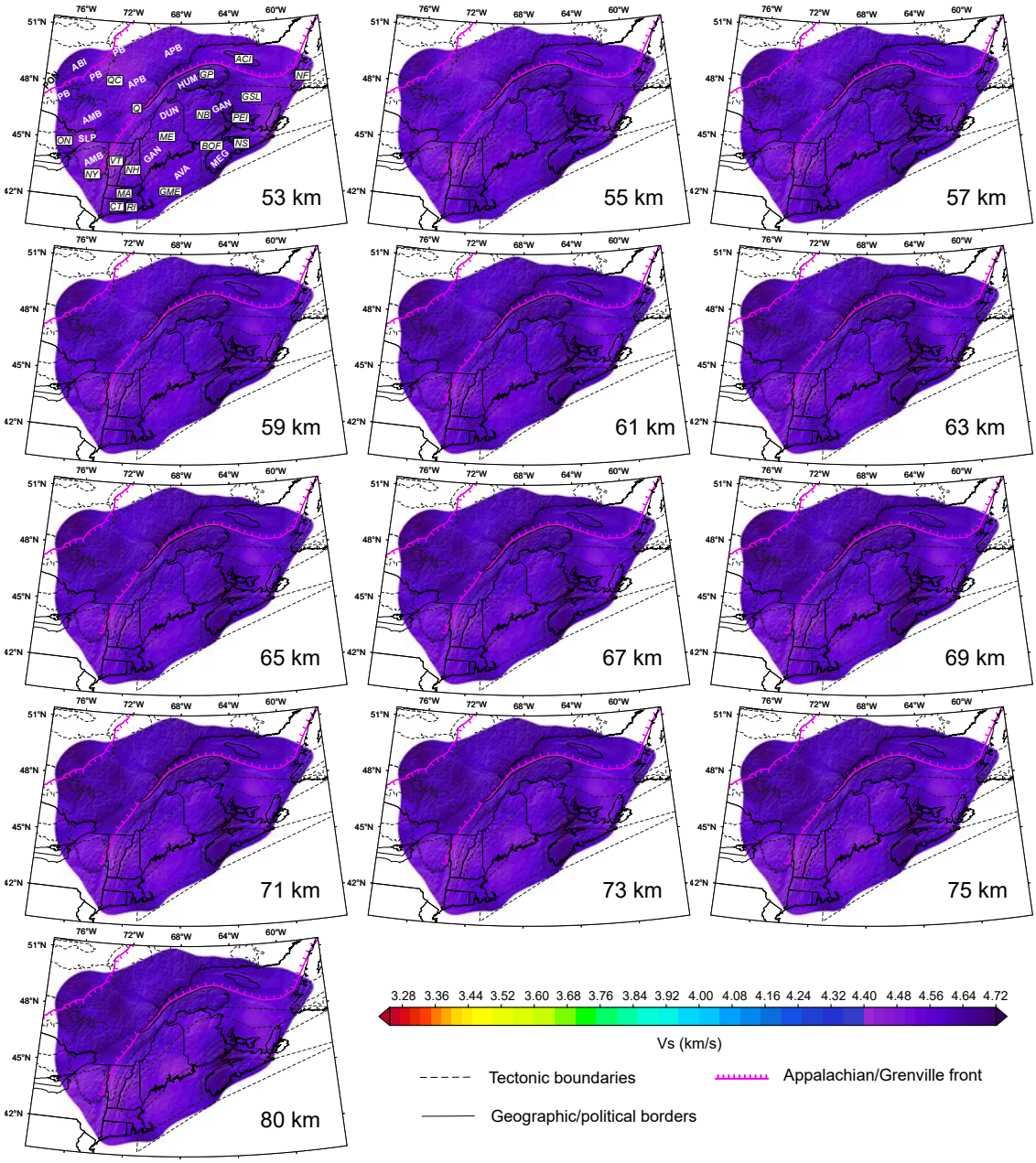

Figure S16. Maps of shear velocity variations at depths from 53 km to 80 km. Acronyms are explained in Figure S12.

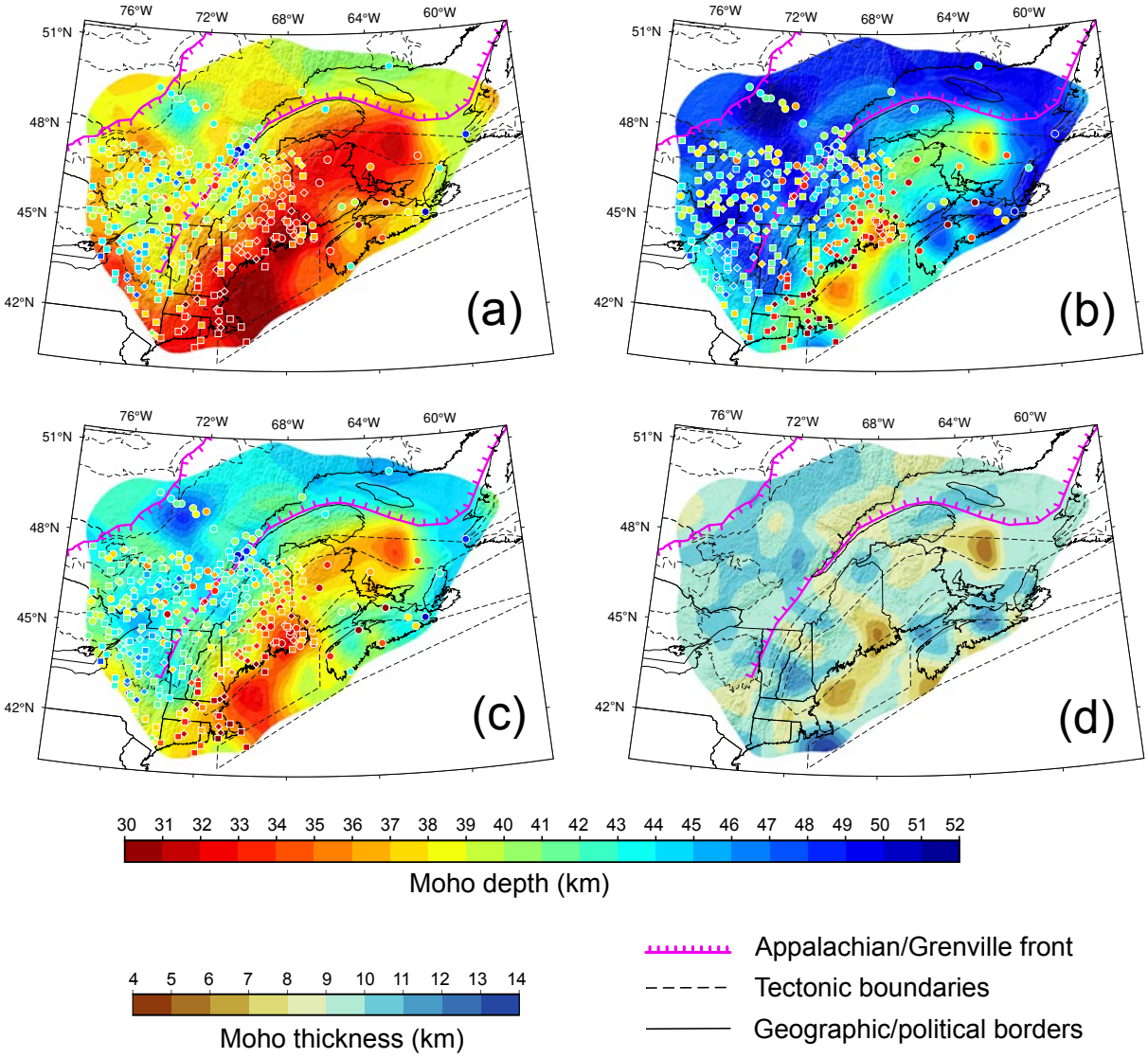

Figure S17. Maps of Moho depths and thickness. (a) Moho depth map obtained using the 50% proxy, (b) Moho depth map obtained using the 85% proxy, (c) Moho depth map obtained by taking the average between the 50% and 85% proxies, (d) Moho thickness map obtained by calculating the difference between the 50% and 85% proxies.

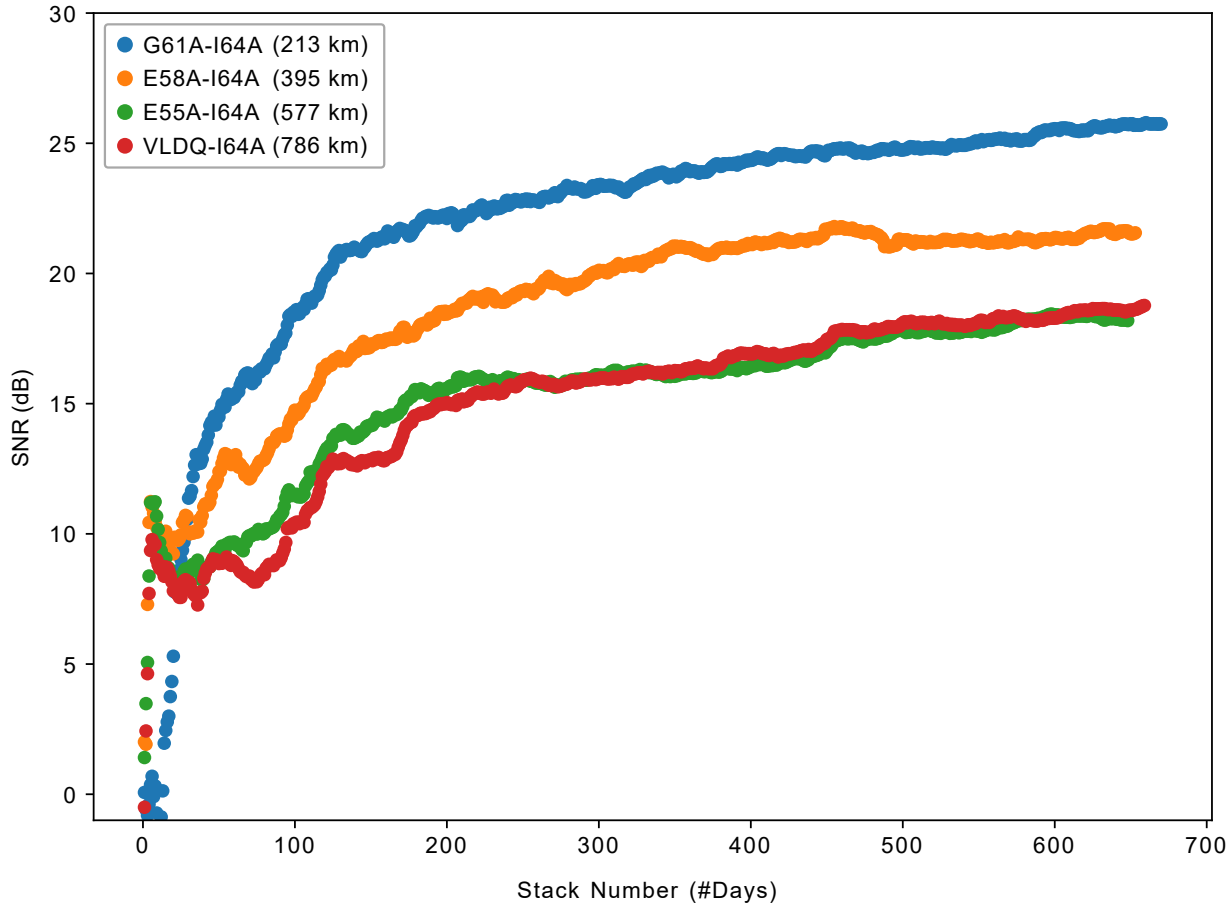

Figure S18. Improvement of EGF signal-to-noise ratios with increasing stack number. The SNR varies depending on the inter-station distance (see legend), but the curves start to stabilize after ∼6 months (∼180 days) of stacking for all cases.

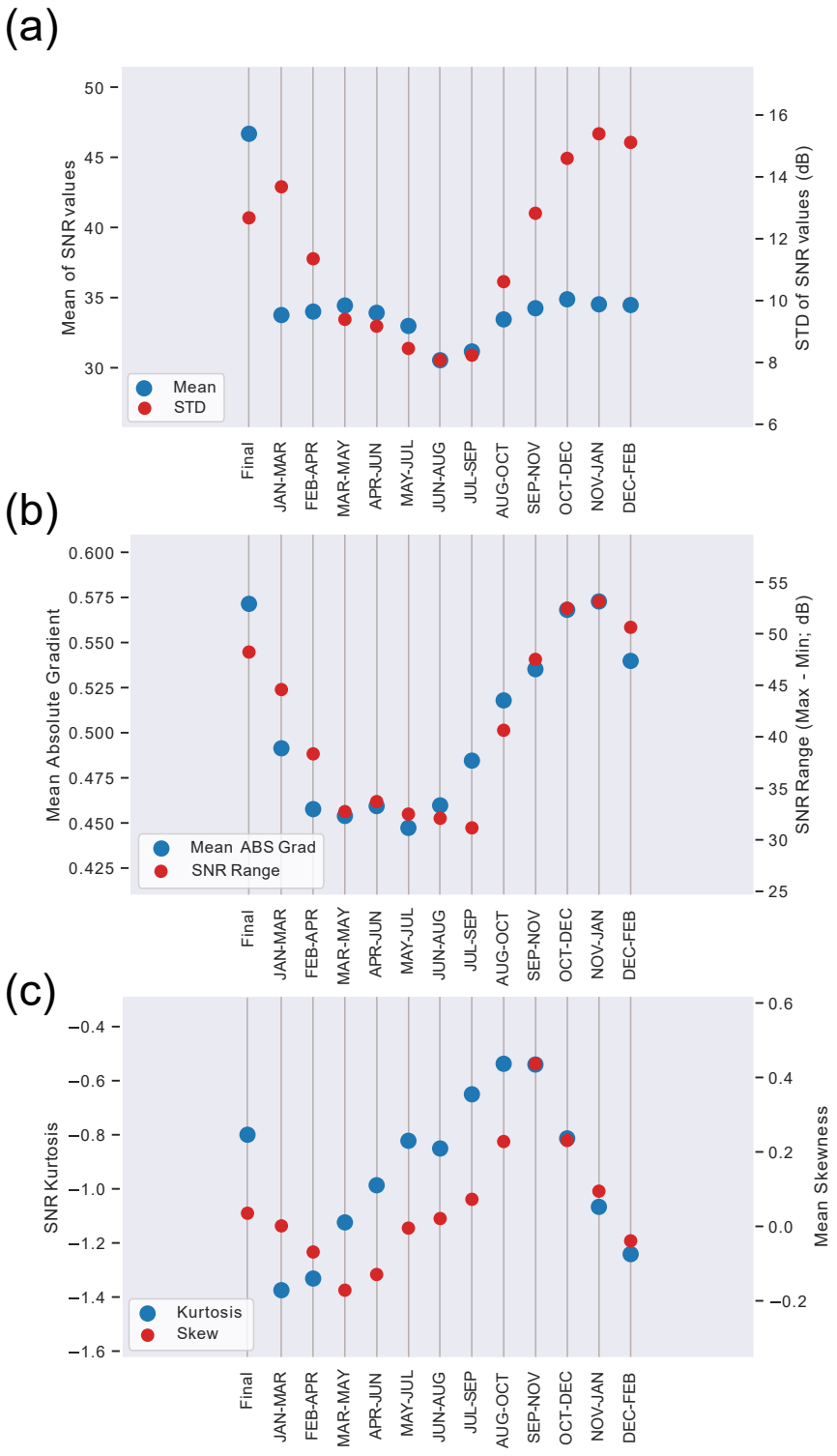

Figure S19. (Caption next page.)

Figure S19. (Previous page.) Statistical parameters for the directionality analysis of different data sets used in this study. For each data set, the propagation directions of causal and acausal signals are considered and the statistical parameters are calculated for the averaged SNR values over 5° azimuthal bins. (a) SNR mean and standard deviation parameters, (b) SNR mean absolute gradient and range (maximum-minimum) parameters, (c) SNR kurtosis (4th standardized moment) and skewness (3rd standardized moment) parameters

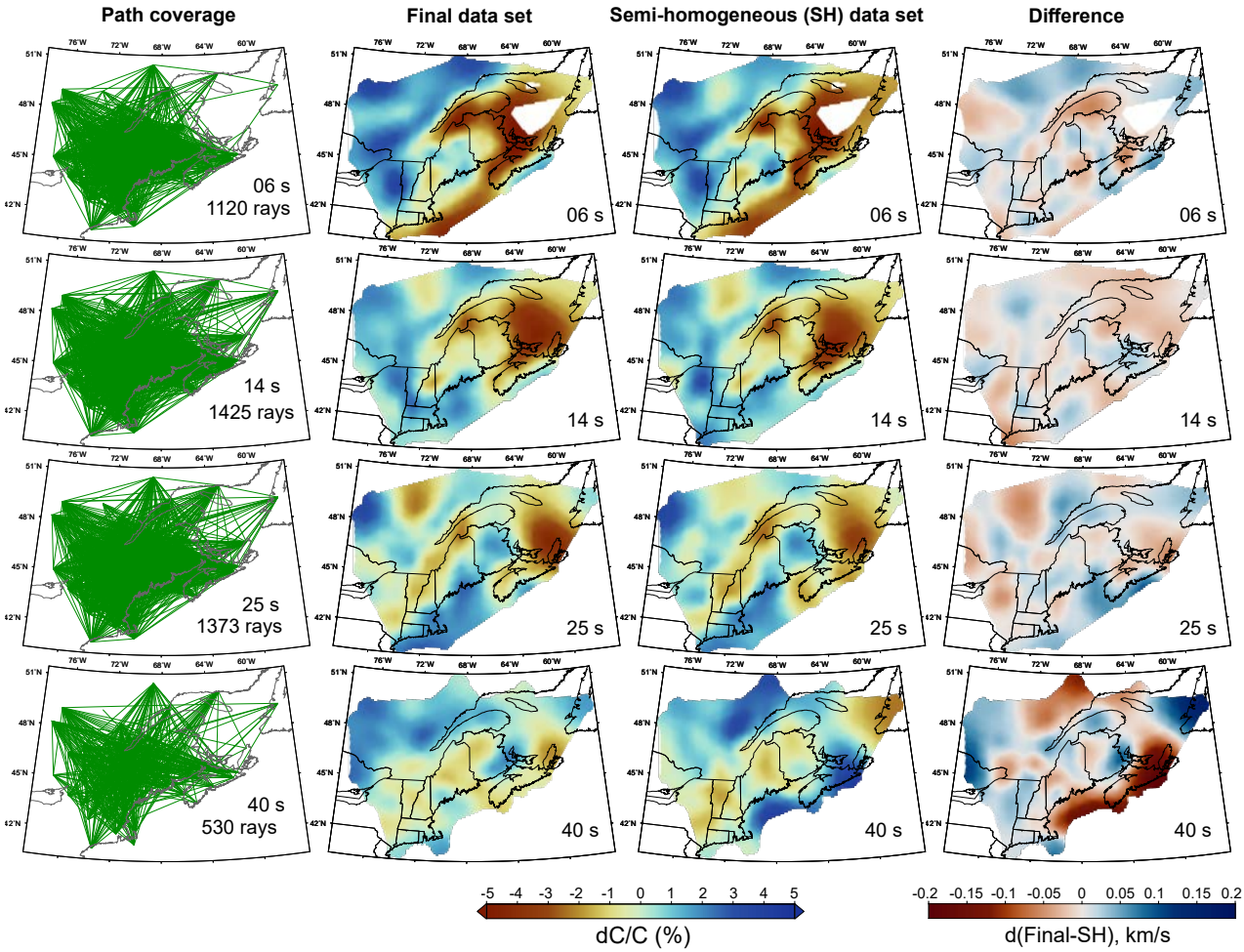

Figure S20. Maps of phase velocities at four representative periods for the test of non-uniform noise distribution effect. The column "Final data set" shows the phase velocity maps obtained from the data used in the generation of final phase velocity maps of this study. The column "Semi-homogenous data set" shows the maps resulting from the "May-July" data that experience the minimum directional bias. The two data sets include exactly the same inter-station paths, illustrated in the left column, to eliminate the effect of path coverage difference. The right column illustrates the difference between the results of the two data sets.

Table S1: Coordinates and details of seismic stations used in this study. Source: http://ds.iris.edu

#	**Station**	**Network**	**Longitude**	**Latitude**	**Elevation (m)**
1	A11	CN	-70.1969	47.2431	55
2	A64	CN	-69.8914	47.8274	132
3	GBN	CN	-61.5128	45.4079	47
4	GGN	CN	-66.8420	45.1184	28
5	HAL	CN	-63.5912	44.6378	65
6	ICQ	CN	-67.2715	49.5223	58
7	LMN	CN	-64.8063	45.8544	365
8	WES	NE	-71.3218	42.3848	60
9	ALLY	Y6	-65.0964	43.7429	12
10	BATG	CN	-66.0599	47.2767	336
11	CHEG	CN	-60.6745	46.8083	443
12	D56A	TA	-74.7568	47.0485	421
13	D59A	TA	-71.8358	47.0073	204
14	D60A	TA	-70.9237	46.9139	40
15	D62A	TA	-69.0501	47.0819	189
16	D63A	TA	-68.1066	47.0370	256
17	DRLN	CN	-57.5032	49.2562	241
18	E55A	TA	-76.0572	46.4538	180
19	E58A	TA	-73.2771	46.3721	233
20	E62A	TA	-69.5227	46.6201	356
21	E64A	TA	-67.8285	46.4184	190
22	EDEY	Y6	-62.3190	45.4409	139
23	EMMW	NE	-67.4573	44.7075	35
24	F57A	TA	-74.6928	45.8122	178
25	F60A	TA	-71.9514	45.9688	229
26	F61A	TA	-70.9921	45.9743	350
27	F62A	TA	-69.9664	45.8968	331
28	F64A	TA	-68.3496	45.8633	179
29	G57A	TA	-74.9855	45.1036	96
30	G59A	TA	-73.1809	45.0807	36
31	G61A	TA	-71.5273	45.2827	378
32	G62A	TA	-70.5319	45.2186	426
33	G63A	TA	-69.6186	45.1147	363
34	H61A	TA	-71.9271	44.5239	462
35	H62A	TA	-71.1559	44.5743	381
36	H63A	TA	-70.0353	44.6616	109
37	H64A	TA	-69.2203	44.6412	158
38	H65A	TA	-68.2469	44.6961	98
39	HANN	PO	-66.7677	45.8818	102
40	HOLY	Y6	-66.4640	46.5259	193
41	I57A	TA	-75.6599	43.9377	321

Table S1: (Continued) Coordinates and details of seismic stations used in this study.

#	**Station**	**Network**	**Longitude**	**Latitude**	**Elevation (m)**
42	I60A	TA	-73.2916	43.8440	101
43	I62A	TA	-71.3359	43.8743	264
44	I63A	TA	-70.5809	44.0505	177
45	I64A	TA	-69.6347	43.9197	17
46	J59A	TA	-74.5041	43.4647	541
47	J62A	TA	-71.8127	43.2262	266
48	J63A	TA	-71.0781	43.2792	142
49	JOSY	Y6	-66.0128	44.2636	76
50	K60A	TA	-73.8886	42.6168	79
51	K62A	TA	-72.2345	42.6651	289
52	L63A	TA	-71.6095	41.8631	109
53	L65A	TA	-70.0528	42.0295	50
54	LATQ	PO	-72.7819	47.3835	163
55	LSQQ	PO	-76.9796	49.0580	308
56	M66A	TA	-70.1353	41.2590	9
57	MALY	Y6	-63.3551	45.7935	33
58	N62A	TA	-73.4677	40.9313	34
59	NATG	CN	-62.8102	50.2872	-2
60	PLVO	PO	-77.0754	45.0396	279
61	QM16	X8	-67.9513	45.2087	126
62	QM38	X8	-70.8531	47.6752	770
63	QM50	X8	-71.6612	48.4079	164
64	QM60	X8	-73.3362	49.1679	354
65	QMM5	X8	-68.7982	50.8438	418
66	SHEY	Y6	-61.9859	45.1324	9
67	SUSY	Y6	-65.4320	45.7174	99
68	VLDQ	CN	-77.7572	48.1901	316
69	WODY	Y6	-64.6629	45.0983	38

Table S2. Final regularization parameters used in the phase velocity inversions.

Period	Smoothing parameters		Damping parameters	
	Isotropic	Anisotropic	Isotropic	Anisotropic
(s)	(C_{iso})	(2ψ and 4ψ)	C_{iso}	(2ψ and 4ψ)
4-50	0.5	0.7	0.05	0.07

Table S3. List of conditions (columns) in the subjective decision of choosing the "semi-homogenous data set". The "May-July" data set is suggested to experience the least directional bias. See Figure S19 for comparison of the statistical parameters.

Dataset	SNR Mean > 32	SNR STD < 10	SNR Grad < 0.475	SNR range < 35	Small negative SNR kurtosis	SNR skewness closest to zero
Final	✓				✓	✓
Jan-Mar	✓					✓
Feb-Apr	✓		✓			
Mar-May	✓	✓	✓	✓		
Apr-Jun	✓	✓	✓	✓		
May-Jul	✓	✓	✓	✓	✓	✓
Jun-Aug		✓	✓	✓	✓	✓
Jul-Sep		✓		✓	✓	✓
Aug-Oct	✓				✓	
Sep-Nov	✓				✓	
Oct-Dec	✓				✓	
Nov-Jan	✓					
Dec-Feb	✓					✓